Silicon Photomultipliers Electrical Model Extensive Analytical Analysis

D. Marano, M. Belluso, G. Bonanno, S. Billotta, A. Grillo, S. Garozzo, G. Romeo, O. Catalano, G. La Rosa, G. Sottile, D. Impiombato, and S. Giarrusso

***Abstract*—The present work aims to address a comprehensive analytical analysis of a new accurate equivalent electrical model of silicon photomultiplier (SiPM) detectors. The proposed circuit model allows to truthfully reproduce the output signal waveform generated by the light sensors apart from the specific technology adopted for the fabrication process, and can also be profitably exploited to perform reliable circuit-level simulations. A detailed and in-depth investigation of the functional parameters involved in the output pulse signals is here developed, and the most significant physical relationships are analytically derived as well. Experimental measurements are finally carried out on real devices, in order to validate the accuracy of the attained expressions, and good fittings are achieved between the analytical curve plots and the associated measurements results. The adopted analysis turns out to be particularly helpful when designing an optimum front-end architecture for SiPM detectors, since the performance of the entire detection system, especially in terms of dynamic range and timing resolution, can be accurately predicted as a function of the SiPM model parameters and the foremost features of the coupled front-end electronics.**

***Index Terms*—Analytical functions, electrical model, equivalent circuits, output current pulses, silicon photomultipliers, time constants, transient waveforms.**

I. Introduction

In line with the contemporary evolution of astrophysics, nuclear science and medical imaging, the realization of silicon photomultiplier detectors is being given an increasingly rising emphasis over recent years. The number of perspective applications exploiting the advantages of solid-state sensors, along with the consequent demand of integrated front-end electronics suitable for this class of photon-detection devices, is continuously growing over time.

Manuscript received December 10, 2012; revised May 14, 2013; accepted September 19, 2013. Date of publication November 11, 2013; date of current version February 06, 2014. This work was supported in part by the ASTRI Flagship Project, financed by the Italian Ministry of Education, University, and Research (MIUR) and led by the Italian National Institute for Astrophysics (INAF).

D. Marano, M. Belluso, G. Bonanno, S. Billotta, A. Grillo, S. Garozzo, and G. Romeo are with INAF, Osservatorio Astrofisico di Catania, I-95123 Catania, Italy (e-mail: dmarano@oact.inaf.it; mbelluso@oact.inaf.it; gbonanno@oact.inaf.it; sbillotta@oact.inaf.it; agrillo@oact.inaf.it; sgarozzo@oact.inaf.it; gromeo@oact.inaf.it).

O. Catalano, G. La Rosa, G. Sottile, D. Impiombato, and S. Giarrusso are with INAF, Istituto di Astrofisica Spaziale e Fisica Cosmica di Palermo, I-90146 Palermo, Italy (e-mail: catalano@ifc.inaf.it; larosa@ifc.inaf.it; sottile@ifc.inaf.it; impiombato@ifc.inaf.it; giarrusso@ifc.inaf.it).

Color versions of one or more of the figures in this paper are available online at http://ieeexplore.ieee.org.

Digital Object Identifier 10.1109/TNS.2013.2283231

Optical semiconductor detectors have been arousing a great interest and are gaining a widespread popularity and diffusion within the scientific community involved in astrophysical and medical fields [1]–[9].

Silicon photomultipliers (SiPMs), also referred to as multi-pixel photon counters (MPPCs), are a relatively novel type of detectors which consist of a parallel array of photon counting microcells including a single-photon avalanche diode (SPAD) and an integrated quenching element. The parallel-connected anodes of the silicon detector deliver an output current signal which is directly proportional to the incident photon flux. The extremely remarkable performance achieved by the SiPM detectors in terms of high photon detection efficiency, fast transient response, excellent timing resolution, and wide spectral range gives them a powerful inherent potential for replacing traditional phototube detectors.

SiPM detectors have been extensively investigated and are now widely developed; the outstanding characteristics offered by most commercially available devices result from new integration concepts and modern semiconductor fabrication techniques. Considerable effort is currently devoted to further improve the high performance achieved by the SiPM detectors. Contextually, the electronics development looks towards the realization of specific and effective front-end architectures.

Owing to the physical structure and operation principles of the SiPM detectors, some of the main issues to be addressed when designing reliable electronic front-end systems concern the dynamic range and the response speed of the current signal produced at the detector output. The front-end electronics acquiring the photo-generated currents is required to preserve and reproduce at its outputs the SiPM electrical signals without significant loading effects or bandwidth restrictions.

Therefore, the first and foremost prerequisite for a successfully designed front-end system is the availability of an accurate electrical model of the SiPM detector which allows a reliable interpretation of its physical interactions with the conditioning electronics, in order to consider a motivated choice of the optimal front-end architecture. A careful theoretical study of both static and dynamic characteristics of the silicon device as a signal source is therefore required. In particular, the total equivalent capacitance as well as the shape of the output pulse produced in response to an incident photon are crucial parameters to be considered for an optimal design and performance assessment of the whole SiPM detection system.

For a thorough analysis and interpretation of SiPM signals a detailed understanding of the physical processes involved is mandatory. A powerful technique to accomplish this target is

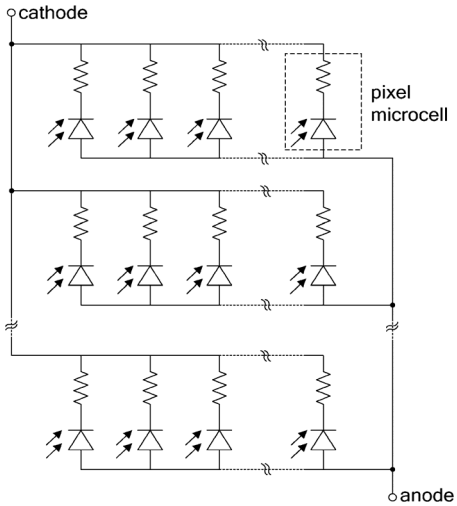

Fig. 1. Simplified equivalent circuit of a SiPM detector as a parallel connection of single basic pixel microcells.

the utilization of equivalent circuit models accurately describing the physical processes experienced by every SiPM microcell. Thanks to these models, reliable circuit-level simulations can be performed on the SiPM detector system coupled to the front-end electronics, and thus the main characteristics of the obtained signals waveforms can be conveniently related to the model parameters of both SiPM detectors and front-end electronics. Of course, the accuracy of simulations depends on the choice of the circuit parameters; nonetheless, on the basis of a complete analytical model, the core physical properties of the SiPM detectors can be functionally associated to the equivalent circuit parameters independently of the particular fabrication technology.

This work develops a detailed analytical investigation of an accurate electrical model of the SiPM detector relying on the static and dynamic behavior of each basic microcell composing the whole detector structure. When hundreds or thousands of microcells are connected in parallel, the current pulses delivered to the external circuitry in response to a photon event are extremely affected by internal and external parasitics and load effects which must be added to the model to properly account for all time constants which characterize the waveforms of the output-generated signals.

Although different SiPM electrical characterizations are reported in literature [1]–[7], a comprehensive analytical study of the achieved model is still missing. An accurate analytical expression of the electrical signal obtained by coupling the detector to the front-end electronics is derived and discussed in detail. Both complete and approximated analytical relationships are provided for the most crucial parameters involved in the circuit model, and the associated curve plots are critically analyzed. Experimental measurements performed on real detectors are finally demonstrated to be in good agreement with the achieved analytical expressions.

It will be shown that the proposed multi-cell model analysis is essential to adequately describe the operation principles of the SiPM detector, since its instantaneous electronic properties are a function of the number of fired and unfired cells. It will be further proved that this functional dependence also results in a strong influence of the front-end input impedance on the proportionality of the output signal.

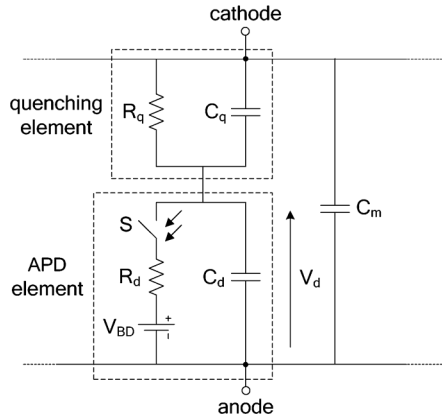

Fig. 2. Equivalent electrical model of a single SPAD microcell.

In Section II the adopted SiPM electrical model is presented. The proposed analytical analysis is carried out in Section III. Measurements results on actual available devices are reported in Section IV. Finally, Section V summarizes the paper conclusions and outlook.

II. SIPM Electrical Model

SiPM detectors basically have a physical structure in which combinations of a Geiger-mode avalanche photodiode micro-pixel and a series quenching resistor are connected in parallel and bi-dimensionally arranged as in Fig. 1. Every elementary microcell independently detects an avalanche event and determines whether a photon has entered the pixel. The output signal produced when one or more photons are detected keeps constant regardless of the number of input photons, meaning that each single SPAD micro-pixel only provides information on whether a photon is received. Since a SiPM detector consists of multiple microcells sharing the same cathode and anode terminals, the output current signal is the sum of all single SPAD currents, therefore indicating the total number of fired microcells. The quenching resistance integrated in each single pixel allows the avalanche current to flow through the photodiode but does not allow a self-sustained avalanche, since it limits the asymptotic steady-state value of this current [2].

All basic micro-pixels are connected to a unique readout channel, so that the current pulses overlap with each other and generate an output signal that is the sum of the currents from each fired SPAD.

The electrical model associated to the elementary microcell is depicted in Fig. 2. The avalanche photodiode is modeled as the parallel connection between the internal resistance of the diode space-charge and quasi-neutral region R_d, and the junction capacitance of the inner depletion layer C_d. The integrated quenching resistor R_q is associated with its parallel stray capacitance C_q, which works as a fast discharging path for the charge delivered during a trigger event. A further parasitic capacitance C_m across the two pixel terminals must be also introduced in the equivalent model of the basic microcell, accounting for the presence of the metal grid paths spanning over the entire surface of the semiconductor device.

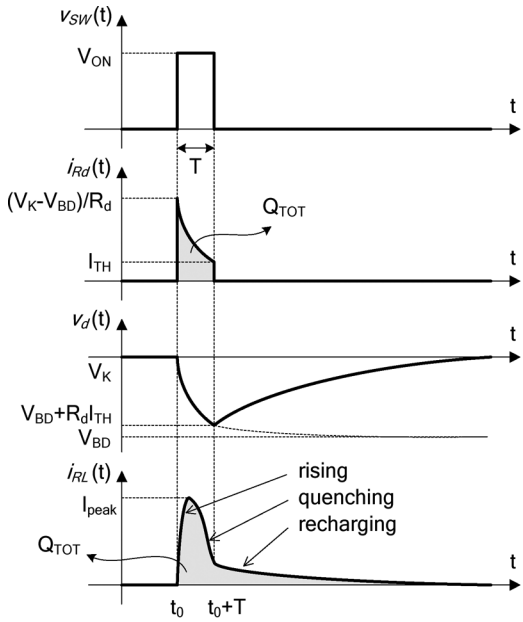

Fig. 3. Characteristic transient current, voltage and output signal waveforms resulting from the adopted SiPM single cell model, with relation to the external switch control voltage simulating a detected event.

The present single-cell model is directly derived by Cova's model in [2], and differs from the equivalent circuit in [3]–[5] in the way the signal charge is engendered. The avalanche following a breakdown event is here modeled by using an ideal DC voltage supply V_{BD} along with a series voltage-controlled switch S, simulating the avalanche triggered by the absorption of one photon. The switch is implemented in such a way that it closes at a preset time t_0, marking the start of a breakdown event. The switch then monitors the current signal generated through the photodiode resistance R_d and opens if this current drops below a predefined threshold value I_{TH}, thus quenching the avalanche process. The switch controlling voltage is realized by a square-wave generator whose pulse width T represents the time interval between the avalanche triggering time t_0 and the instant at which the single photodiode current decreases below the threshold level. This threshold current is commonly referred to as latching current [2], and represents the minimum current amplitude which is able to self-sustain the avalanche process. Therefore, the diode quenching time can be considered to be the instant at which the exponentially decaying current across R_d reaches the latching current. Subsequently, the photodiode enters the recharging operation, and the transient voltage across its terminals slowly rises over V_{BD} towards the external cathode bias voltage.

The transient current and voltage waveforms, namely $i_{Rd}(t)$ and $v_d(t)$, respectively, resulting from the adopted photodiode equivalent model when its anode is connected to a load resistor R_L, are illustrated in Fig. 3 with relation to the external pulse-wise voltage $v_{SW}(t)$, applied to the control switch and producing the trigger event. In addition, the current signal $i_{RL}(t)$ through the output load is also shown. Its typical behavior consists of three succeeding intervals: rising, quenching, and recharging. The rise (onset) phase corresponds to the time interval required by the inner photodiode avalanche to be transferred to the output load resistor; the quenching period occurs between the diode current peak value and the instant at which the diode current R_d becomes zero; the third range originates from the slow recharging of the equivalent diode capacitances through the quenching resistor R_q. Primary aim of the following analysis is to provide a systematic analytical characterization of these single physical phases constituting the complete SiPM electrical output response.

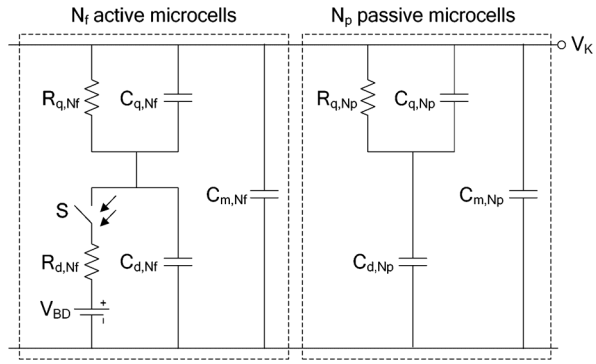

Fig. 4. Equivalent circuit of the overall SiPM architecture.

As will be shortly discussed, the choice of the above charge generation model results in an accurate description of all typical transient processes consequent to the detection of a trigger event. Conversely, the equivalent circuits employing a current source as a Dirac's delta pulse to simulate the avalanche process might be intrinsically limited for a correct assessment of the rising, quenching and recharging phases characterizing the output current pulse in response to a detected event.

The electrical model in Fig. 2 can be easily extended to the case in which more than one microcell is interested by an avalanche event by simply connecting in parallel multiple SPAD elements. The full equivalent model simulating the discharge of N_f active microcells for a SiPM detector consisting of a total number of N microcells is illustrated in Fig. 4, where the dashed lines separate the circuit into an active part representing the N_f fired pixels and a passive component standing for the remaining $N_p = N - N_f$ unfired microcells.

A further fringe capacitance modeling the cathode bonding pad of the whole detector should be included in the schematic model, but its effects can be endorsed in the parallel contribution of C_m for each single microcell.

The i-th equivalent resistances and capacitances included in the active and passive parts of the full SiPM detector model in Fig. 4 are expressed by the following relationships

$$R_{i,N_f} = \frac{R_i}{N_f},\ R_{i,N_p} = \frac{R_i}{N_p},\ C_{i,N_f} = N_f C_i,\ C_{i,N_p} = N_p C_i \tag{1}$$

Based on the complete SiPM electrical model in Fig. 4, the proposed analytical analysis is now discussed.

III. SIPM Model Analytical Analysis

Two distinct transient analyses are now carried out for the two dynamic phases preceding and succeeding the opening of the control switch at $t = T$.

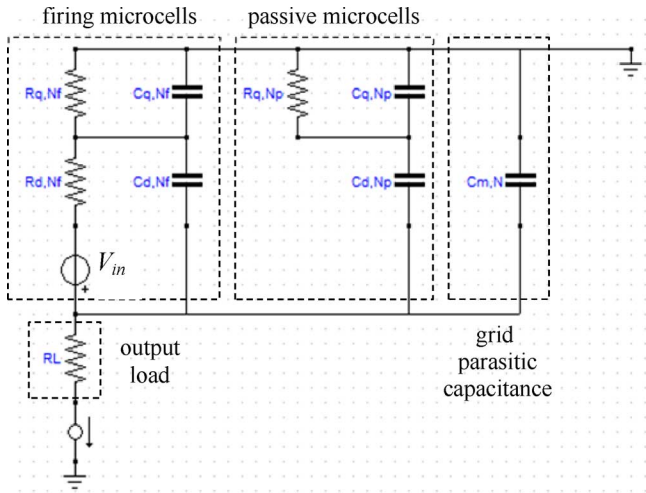

Fig. 5. Linearized small-signal equivalent circuit of the SiPM detector.

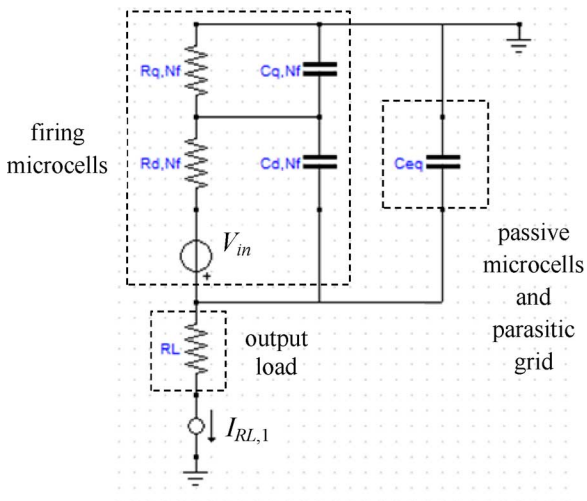

Fig. 6. Simplified small-signal schematic used for the evaluation of the SiPM output current frequency response for the rising and quenching operations.

A. Rising and Quenching Operations

Fig. 5 depicts the linearized small-signal equivalent circuit used for deriving the Laplace-domain analytical expression of the output current signal across the load resistor R_L during the first part of the transient response, prior to the quenching time T. The constant potential V_K is grounded, the voltage source V_{BD} is short-circuited, the parallel-connected capacitors $C_{m,Nf}$ and $C_{m,Np}$ are grouped together into a single equivalent contribution $C_{m,N} = NC_m$, and an AC output current probe is added to the circuit as a read-out signal.

As previously stated, the rising and quenching parts of the SiPM output current $i_{RL}(t)$ in response to a photon event occur starting from the first closing of the control switch, at the initial time $t_0 = 0$, and persist as long as it remains in its on-state condition for a prefixed time $t = T$, established by the tunable pulse-width of the controlling voltage v_{SW}. During this period of time, a constant voltage $V_{OV} = V_K - V_{BD}$, also known as overvoltage or excess bias voltage, is applied to the circuit and is responsible for the current generation through the diode internal equivalent resistance $R_{d,Nf}$. Hence, prior to the quenching time T, the switch can be assumed to be replaced by a voltage source V_{in} with a step function of amplitude V_{OV}.

A qualitative study of the circuit can be carried out without losing accuracy by referring to the simplified schematic illustrated in Fig. 6, in which the impedance offered by the parallel connection of $R_{q,Np}$ and $C_{q,Np}$ is supposed to be merely due to the capacitive elements of the unfired microcells, so that an equivalent capacitor C_{eq} can conveniently model the contributions of $C_{q,Np}$, $C_{d,Nf}$ and $C_{m,N}$ according to

$$C_{eq} = \frac{C_{d,N_p} C_{q,N_p}}{C_{d,N_p} + C_{q,N_p}} + C_{m,N} = (N - N_f)\frac{C_d C_q}{C_d + C_q} + NC_m \tag{2}$$

The foregoing assumption holds true during the fast rising and quenching operations, and is further fulfilled provided that the front-end input resistance R_L is much lower than $R_{q,Np}$.

The small-signal transconductance transfer function of the circuit in Fig. 6 as a function of the complex frequency is

$$H_{R_L}(s) = \frac{I_{R_L,1}(s)}{V_{in}(s)} = H_0 \frac{1 + s\tau_q}{1 + a_1 s + a_2 s^2} \tag{3}$$

where $H_0 = N_f/(R_q + R_d + N_f R_L)$, $\tau_q = R_q C_q$, whilst the s-coefficients of the second-order polynomial in the denominator are given by the following expressions

$$a_1 = \frac{R_d C_d (R_q + N_f R_L) + R_q C_q (R_d + N_f R_L) + C_{eq} R_L (R_q + R_d)}{R_q + R_d + N_f R_L} \tag{4}$$

$$a_2 = \frac{R_d R_q R_L}{R_q + R_d + N_f R_L} \left[C_{eq}(C_d + C_q) + N_f C_d C_q \right] \tag{5}$$

Since ${a_1}^2 > a_2$, the above transfer function exhibits two real poles and can be more conveniently expressed as

$$H_{R_L}(s) = \frac{I_{R_L,1}(s)}{V_{in}(s)} = H_0 \frac{1 + s\tau_q}{(1 + s\tau_i)(1 + s\tau_d)} \tag{6}$$

where the associated time constants are related to the denominator s-coefficients according to the following relationships

$$\tau_i = \frac{2a_2}{a_1 + \sqrt{{a_1}^2 - 4a_2}} \tag{7}$$

$$\tau_d = \frac{2a_2}{a_1 - \sqrt{{a_1}^2 - 4a_2}} \tag{8}$$

The circuit time constants τ_i and τ_d respectively account for the rising and quenching processes undergone by the generated avalanche current through the SiPM output terminals.

Considering $V_{in}(s) = V_{OV}/s$ in (6), yields

$$I_{R_L,1}(s) = H_{R_L}(s) V_{in}(s) = V_{OV} H_0 \frac{1 + s\tau_q}{s(1 + s\tau_i)(1 + s\tau_d)} \tag{9}$$

from which, by easily inverse Laplace transforming, the SiPM output current during the rising and quenching transient operations can be derived as a function of time

$$i_{R_L,1}(t) = I_f \left(1 - \frac{\tau_q - \tau_i}{\tau_d - \tau_i} e^{-\frac{t}{\tau_i}} + \frac{\tau_q - \tau_d}{\tau_d - \tau_i} e^{-\frac{t}{\tau_d}} \right) \tag{10}$$

where I_f is the current final value expressed by

$$I_f = H_0 V_{OV} = N_f \frac{V_{OV}}{R_q + R_d + N_f R_L} \tag{11}$$

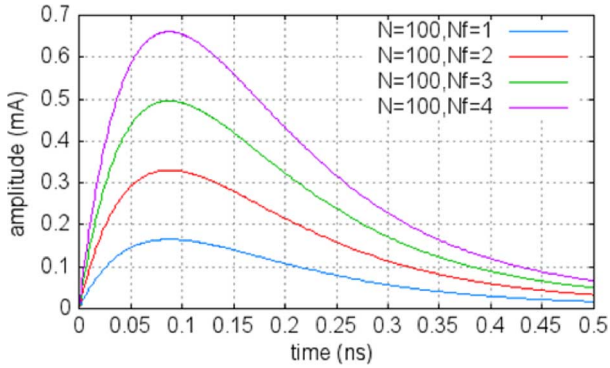

Fig. 7. Analytical SiPM output current waveforms upon a 50-Ω load resistor during the rising and quenching phases, for $V_{OV} = 2$ V, $N = 100$, and growing values of the firing cells ($R_d = 300\ \Omega$, $R_q = 300$ kΩ, $C_d = 200$ fF, $C_q = 20$ fF, $C_m = 5$ fF).

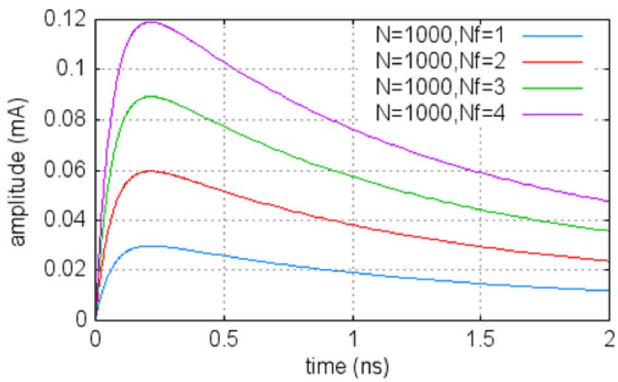

Fig. 8. Analytical SiPM output current waveforms upon a 50-Ω load resistor during the rising and quenching phases, for $V_{OV} = 2$ V, $N = 1000$, and growing values of the firing cells ($R_d = 300\ \Omega$, $R_q = 300$ kΩ, $C_d = 200$ fF, $C_q = 20$ fF, $C_m = 5$ fF).

to which the current pulses would asymptotically tend at the end of the transient quenching phase if the avalanche generation process was not previously self-quenched.

The obtained current waveforms on a 50-Ω load resistor are graphically plotted for $V_{OV} = 2$ V and typical model parameters ($R_d = 300\ \Omega$, $R_q = 300$ kΩ, $C_d = 200$ fF, $C_q = 20$ fF, $C_m = 5$ fF). In Fig. 7 and Fig. 8 the output current pulses, respectively for $N = 100$ and $N = 1000$, are reported for increasing values of the number of fired cells N_f. As can be inspected, the current curves show a fast upward-sloping transient until a peak value is reached, and afterwards exponentially decay with a relatively slower time constant, tending to the asymptotic value I_f.

Both rising and quenching time constants are proved to be negligibly affected by the number of active microcells. On the other hand, their functional dependence on the overall SiPM cells number is depicted in Fig. 9, for the rising phase, and in Fig. 10, for the quenching counterpart.

To perform a first-order analytical assessment of the two characteristic time constants and provide a graphical comparison with the related curve plots, observing (3) and (6) yields $a_1 = \tau_i + \tau_d$ and $a_2 = \tau_i \tau_d$, from which, assuming $\tau_i \ll \tau_d$, leads to

$$\tau_i \approx \frac{a_2}{a_1} \tag{12}$$

$$\tau_d \approx a_1 \tag{13}$$

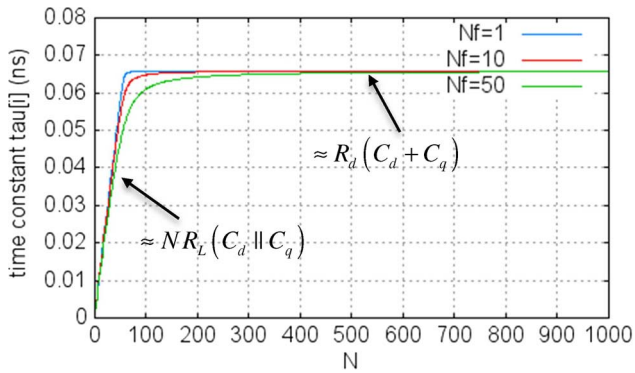

Fig. 9. Rising time constant of the SiPM output current waveforms upon a 50-Ω load resistor as a function of N for different values of N_f ($R_d = 300\ \Omega$, $R_q = 300$ kΩ, $C_d = 200$ fF, $C_q = 20$ fF, $C_m = 5$ fF).

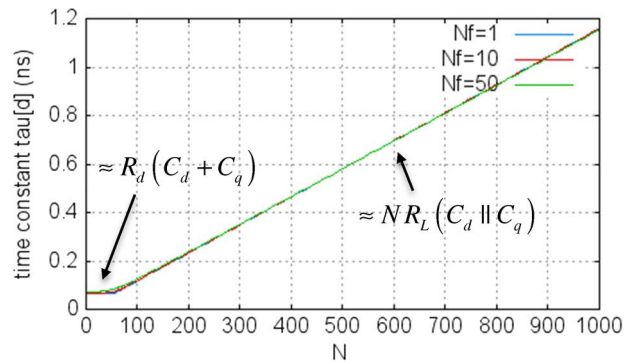

Fig. 10. Quenching time constant of the SiPM output current waveforms upon a 50-Ω load resistor as a function of N for different values of N_f ($R_d = 300\ \Omega$, $R_q = 300$ kΩ, $C_d = 200$ fF, $C_q = 20$ fF, $C_m = 5$ fF).

Moreover, considering $R_q \gg N_f R_L$, $R_q \gg R_d$, and $N \gg N_f$ in (4) and (5), and also neglecting the small contribution of C_m, entails

$$a_1 \approx R_d(C_d + C_q) + NR_L(C_d \| C_q) \tag{14}$$

$$a_2 \approx NR_d R_L C_d C_q \tag{15}$$

from which the approximated time constants simplify into

$$\tau_i \approx \frac{NR_d R_L C_d C_q}{R_d(C_d + C_q) + NR_L(C_d \| C_q)} \tag{16}$$

$$\tau_d \approx R_d(C_d + C_q) + NR_L(C_d \| C_q) \tag{17}$$

where $C_d \| C_q$ is the equivalent capacitance $C_d C_q/(C_d + C_q)$, resulting from the series connection of C_d and C_q.

From the foregoing relationships and by a direct inspection of the family curves in Fig. 9 and Fig. 10, it turns out that the rising time constant presents a first slightly linear growth for increasing values of N, as long as the second term in the denominator of (16) can be neglected, and approximately tends to the constant value of $R_d(C_d + C_q)$ for a large number of cells, when the first term is instead negligible; on the other side, the quenching time constant assumes a nearly constant value for a low number of cells, according to (17), while raises up with a roughly constant slope of $R_L(C_d \| C_q)$ for higher values of N.

Fig. 11 illustrates the functional dependence of the detector current time waveforms on the total number of microcells of which the device is constituted, for a single photon detected.

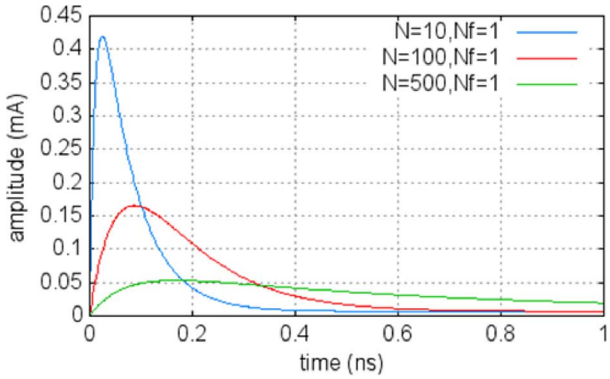

Fig. 11. Analytical SiPM output current waveforms upon a 50-Ω load resistor during the rising and quenching operations, for $V_{OV} = 2$ V, $N_f = 1$, and growing values of N ($R_d = 300\ \Omega$, $R_q = 300$ kΩ, $C_d = 200$ fF, $C_q = 20$ fF, $C_m = 5$ fF).

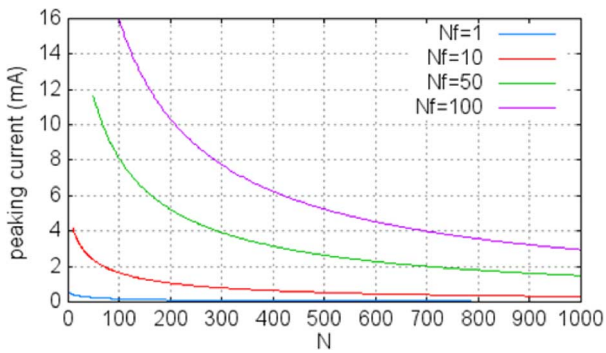

Fig. 12. Analytical SiPM peak current curves upon a 50-Ω load resistor as a function of N for $V_{OV} = 2$ V and different values of N_f ($R_d = 300\ \Omega$, $R_q = 300$ kΩ, $C_d = 200$ fF, $C_q = 20$ fF, $C_m = 5$ fF).

As expected, for raising values of N, the single output current pulse decreases its peaking current and enlarges the associated time constants in good agreement with the approximated expressions in (16) and (17). In fact, all passive microcells act as a low-pass filter for the output signal generated by one single fired cell. Besides, all time curves in Fig. 11 would approach the same asymptotic current I_f for any value of N. So, in keeping with the charge conservation principle, the integral of the output current waveforms with respect to time, which represents the charge injected by the firing SiPM microcells, remains constant regardless of N, as can be also shown by assessing the surface area of the part of the plane lying beneath the output current functions.

The peaking current and the corresponding peaking time of the SiPM output current waveforms can be obtained by nullifying the first derivative in (10), leading to

$$I_{peak} = I_f \left\{ 1 + \frac{\tau_q - \tau_d}{\tau_d} \left[\frac{\tau_i(\tau_q - \tau_d)}{\tau_d(\tau_q - \tau_i)} \right]^{\frac{\tau_i}{\tau_d - \tau_i}} \right\} \quad (18)$$

$$T_{peak} = \frac{\tau_d \tau_i}{\tau_d - \tau_i} \log \left[\frac{\tau_d(\tau_q - \tau_i)}{\tau_i(\tau_q - \tau_d)} \right] \quad (19)$$

In order to illustrate the functional relationships of I_{peak} and T_{peak} on the total number of microcells, the above expressions are plotted as a function of N for different values of N_f. In Fig. 12 and Fig. 13 the resulting parametric plots are reported,

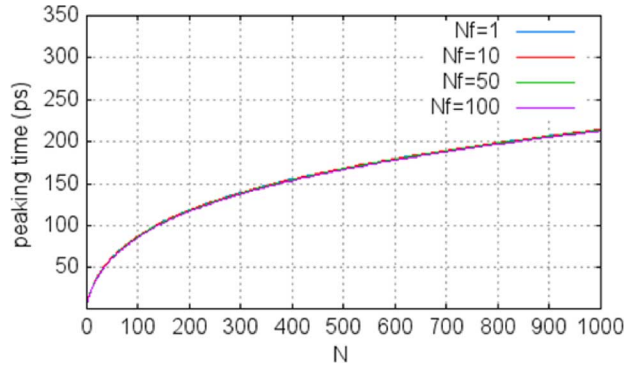

Fig. 13. Analytical SiPM peak time curves upon a 50-Ω load resistor as a function of N for $V_{OV} = 2$ V and different values of N_f ($R_d = 300\ \Omega$, $R_q = 300$ kΩ, $C_d = 200$ fF, $C_q = 20$ fF, $C_m = 5$ fF).

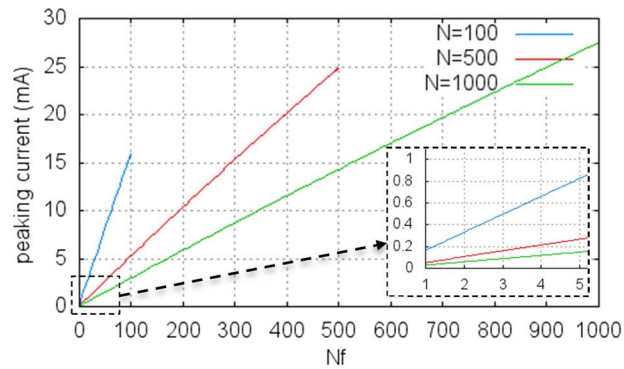

Fig. 14. Analytical peak amplitudes of the SiPM current waveforms upon a 50-Ω load resistor as a function of N_f for $V_{OV} = 2$ V and different values of N ($R_d = 300\ \Omega$, $R_q = 300$ kΩ, $C_d = 200$ fF, $C_q = 20$ fF, $C_m = 5$ fF).

respectively for I_{peak} and T_{peak}, upon $V_{OV} = 2$ V and $R_L = 50\ \Omega$.

By inspection of Fig. 12, it can be noticed that the peaking current of the output pulses exponentially decays for increasing values of N, as a result of the low-pass filter action on the produced signal; simultaneously, as revealed by Fig. 13, the instants at which the peaks occur logarithmically increase so as to maintain the pulse surface area constant, in confirmation of the effective behavior discernable by the time functions in Fig. 11. Furthermore, for a fixed value of N, the peaking time of the current pulses is not significantly affected by the number of firing cells, as also confirmed by the time curves in Fig. 7 and Fig. 8, while the relevant current peaks expectedly raise up with increasing numbers of fired microcells.

In order to better examine the proportionality occurring between the incident photons and the current peak amplitude of the SiPM output signal, in Fig. 14 the direct peaking current dependence on N_f is illustrated for different values of N. For a particular number of total microcells, a good linearity is achieved, by means of which the number of photons detected by the SiPM system can be correctly estimated.

Assuming $\tau_i \ll \tau_d \ll \tau_q$, which is a feasible condition for typical model parameters, the I_{peak} formula in (18) reduces to

$$I_{peak} \approx I_f \left[1 + \frac{\tau_q - \tau_d}{\tau_d} \left(\frac{\tau_i}{\tau_d} \right)^{\frac{\tau_i}{\tau_d}} \right] \approx I_f \frac{\tau_q}{\tau_d} \quad (20)$$

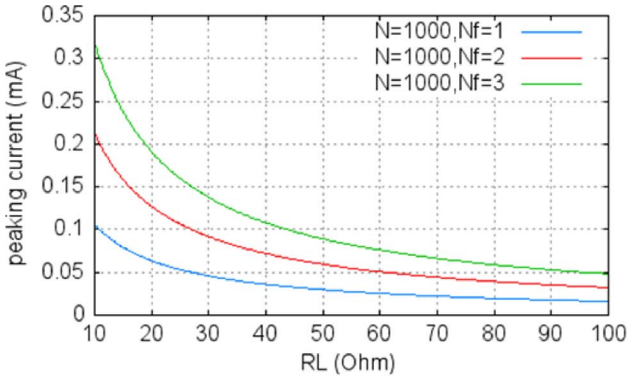

Fig. 15. Analytical peak amplitudes of the SiPM output current pulse as a function of the load resistor R_L, for $V_{OV} = 2$ V, $N = 1000$, and increasing values of N_f ($R_d = 300\ \Omega$, $R_q = 300$ kΩ, $C_d = 200$ fF, $C_q = 20$ fF, $C_m = 5$ fF).

Substituting expressions (11) and (17) into the previous relationship, and considering $R_{q,Nf} \gg R_L$, yields

$$I_{peak} \approx \frac{N_f V_{OV} C_q}{R_d(C_d + C_q) + N R_L (C_d \| C_q)} \tag{21}$$

in which the linear proportionality to N_f is made explicit.

As can be above distinguished in Fig. 14, the angular coefficient of the I_{peak} functions versus N_f gets reduced for increasing values of N. Most importantly, the peak amplitude of the output pulses also depends on the load resistance R_L. For very small values of N, the second addend in the denominator of (21) can be neglected with respect to the first term, leading to the approximated value $I_{peak} = N_f V_{OV}/R_d(1+C_d/C_q)$, which is also reported in [1] and [2] for a single SPAD cell. Conversely, detectors with a large number of total cells may result in a sensible influence of the front-end input resistance upon the peak values of their current signals. This ought to be carefully considered, especially when dealing with current-mode front-end systems acquiring the SiPM output current pulses.

To this regard, Fig. 15 depicts the peaking current I_{peak} as a function of R_L, for $V_{OV} = 2$ V, $N = 1000$, and increasing values of N_f. An almost hyperbolic behavior of the current peak amplitudes is observed from the plotted graphs, which is quite consistent with the achieved expression in (21).

This functional relationship is also reflected in the output voltage pulses produced by the SiPM current signals flowing through the load resistance. In fact, the transient curves of the pulse-like voltage $V_{RL}(t) = R_L i_{RL}(t)$ are simply vertically upward translated by a factor R_L, compared to the current waveforms in Fig. 7 and Fig. 8, but their peak amplitudes $V_{peak} = R_L I_{peak}$ are still functions of the load resistor R_L. However, a remarkably lower dependence of V_{peak} on R_L is now inferred for large values of N. Concerning this aspect, Fig. 16 reports the peak functions of the voltage response $V_{RL}(t)$ versus R_L, for a single firing cell and different numbers of total pixels, by inspection of which a smoother slope is detected for those functions with larger values of N. So, the voltage pulse response of high density cells detectors is less sensitive to variations of the front-end electronic input resistance.

Besides, the peaking time of the output current and voltage waveforms in (19) is found to be marginally affected by variations in R_L.

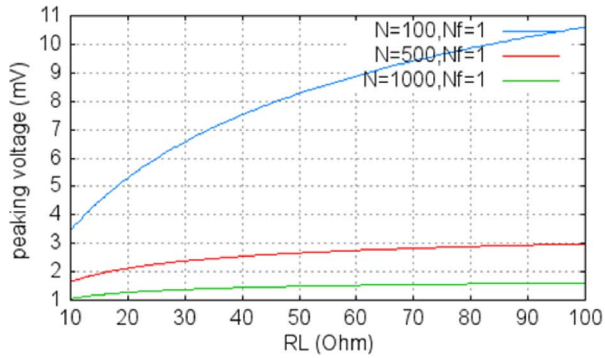

Fig. 16. Analytical peak amplitudes of the SiPM output voltage pulse as a function of the load resistor R_L, for $V_{OV} = 2$ V, $N_f = 1$, and different values of N ($R_d = 300\ \Omega$, $R_q = 300$ kΩ, $C_d = 200$ fF, $C_q = 20$ fF, $C_m = 5$ fF).

B. Quenching Time Evaluation

Hitherto, most attention in the present analysis has been focused on the SiPM output current through the load resistor R_L, which is definitely the electrical signal to be processed by the front-end electronics. Nonetheless, the two distinct transitions of the output response in Fig. 3 are clearly demarcated by the time instant T, when the current through the diode resistance R_d approaches the minimum current level I_{TH} maintaining the fluctuation of carriers during the avalanche process. After a time period T from a trigger event, the multiplication factor of the electron-hole pairs generation equals unity, such that the avalanche current through the diode cannot be self-sustained any longer, and the output response across the load resistance undertakes a different dynamic behavior.

It should be noted, however, that the threshold current I_{TH}, and, in turn, the associated quenching time T, is not a sharply defined quantity, due to the statistical nature of the avalanche generation process, although a virtual average value of 100 μA has commonly been adopted in literature as the latching current of a single SPAD microcell [2].

In order to provide a first-order estimation for the adopted model, which may be helpful for comparisons among different circuit topologies, the quenching time of the SiPM output pulses can be assumed to be the instant at which the current through the equivalent resistance $R_{d,Nf}$ crosses the predefined threshold level $I_{TH,Nf} = N_f I_{TH}$, dictated by the average quenching current of an individual microcell as well as by the number of firing cells.

To this purpose, an analytical expression for the time function $i_{Rd}(t)$ is here derived, by means of which the quenching time of the SiPM output response can be roughly evaluated.

Applying the output current probe in Fig. 6 in series with the diode equivalent resistance $R_{d,Nf}$, the resulting small-signal transfer function is found to be

$$H_{R_d}(s) = \frac{I_{R_d}(s)}{V_{in}(s)} = H_0 \frac{1 + a_1' s + a_2' s^2}{1 + a_1 s + a_2 s^2} \tag{22}$$

where the s-coefficients of the second-order polynomial in the numerator are expressed by

$$a_1' = \lim_{R_d \to +\infty} a_1 = R_q(C_d + C_q) + R_L(C_{eq} + N_f C_d) \tag{23}$$

$$a_2' = \lim_{R_d \to +\infty} a_2 = R_q R_L \left[C_{eq}(C_d + C_q) + N_f C_d C_q\right] \tag{24}$$

Since $a_1'^2 > a_2'$, the former transfer function can be usefully rewritten in a similar way as in (6), implying

$$H_{R_d}(s) = \frac{I_{R_d}(s)}{V_{in}(s)} = H_0 \frac{(1+s\tau_{i2})(1+s\tau_{d2})}{(1+s\tau_i)(1+s\tau_d)} \tag{25}$$

where the new time constants in the numerator are given by

$$\tau_{i2} = \frac{2a_2'}{a_1' + \sqrt{a_1'^2 - 4a_2'}} \tag{26}$$

$$\tau_{d2} = \frac{2a_2'}{a_1' + \sqrt{a_1'^2 - 4a_2'}} \tag{27}$$

As will be shortly addressed, τ_{i2} and τ_{d2} represent the reciprocal of the frequency poles characterizing the detector output current response during the subsequent recharging operation, when no current flows through the equivalent resistor $R_{d,Nf}$.

Assuming, as in (9), the same voltage step function of amplitude V_{OV} for the input source generator V_{in}, yields

$$I_{R_d}(s) = H_{R_d}(s)V_{in}(s) = V_{OV}H_0 \frac{(1+s\tau_{i2})(1+s\tau_{d2})}{s(1+s\tau_i)(1+s\tau_d)} \tag{28}$$

from whose inverse Laplace transform, the current $i_{Rd}(t)$ can be obtained as a function of time

$$i_{R_d}(t) = I_f \left[1 + \frac{(\tau_{d2}-\tau_i)(\tau_{i2}-\tau_i)}{\tau_i(\tau_d-\tau_i)} e^{-\frac{t}{\tau_i}} - \frac{(\tau_{d2}-\tau_d)(\tau_{i2}-\tau_d)}{\tau_d(\tau_d-\tau_i)} e^{-\frac{t}{\tau_d}}\right] \tag{29}$$

The total charge released by the avalanche starting from the initial time $t = 0$ is collected across the equivalent resistor $R_{d,Nf}$ until the quenching time T. Just after the switch is closed, the current $i_{Rd}(t)$ abruptly jumps to its peak value $i_{Rd}(0) = V_{OV}/R_{d,Nf}$ and exponentially drops towards the asymptotic steady-state value I_f with the same time constants as $i_{RL,1}(t)$.

Since the avalanche current is only related to the charge delivered by the fired cells, the $i_{Rd}(t)$ expression in (29) is directly proportional to the active cells N_f and does not depend on N_p. Thus, for a fixed value of N_f, its functional dependence on the overall number of microcells is marginal.

Moreover, for a given number of firing cells, as I_f is well beyond the threshold level $I_{TH,Nf}$, the avalanche discharge current interrupts when the slower time constant τ_d still has no effect on the transient behavior of i_{Rd}; as a consequence, for $t < T$, expression (29) is well approximated by

$$i_{R_d}(t) \approx I_f \left[1 + \frac{(\tau_{d2}-\tau_i)(\tau_{i2}-\tau_i)}{\tau_i(\tau_d-\tau_i)} e^{-\frac{t}{\tau_i}}\right] \tag{30}$$

from which, by setting $I_{Rd}(T) = N_f I_{TH}$, the quenching time T can be easily assessed for a fixed value of I_{TH}, yielding

$$T = \tau_i \log\left[\frac{(\tau_{d2}-\tau_i)(\tau_{i2}-\tau_i)}{\tau_i(\tau_d-\tau_i)}\left(\frac{I_f}{N_f I_{TH} - I_f}\right)\right] \tag{31}$$

Fig. 17 illustrates the dynamic $i_{Rd}(t)$ functions for $V_{OV} = 2$ V, $I_{TH} = 100$ μA, and raising values of N_f. As better outlined in the enlarged box, the declining avalanche currents cross the latching levels with a fairly consistent slope, so that

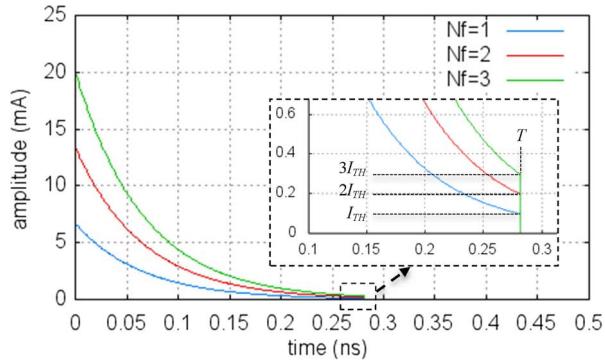

Fig. 17. Analytical current waveforms across the diode equivalent resistance $R_{d,Nf}$, for increasing values of the fired microcells, for $N = 1000$, $V_{OV} = 2$ V, and $I_{TH} = 100$ μA ($R_d = 300$ Ω, $R_q = 300$ kΩ, $C_d = 200$ fF, $C_q = 20$ fF, $C_m = 5$ fF).

the avalanche process is neatly quenched after a time $t = T$, which is typically valued in the range of a few hundreds of picoseconds.

The quenching time T in (31) is found to be marginally affected by the number of fired cells N_f, especially for high values of N, and is solely related to the SiPM model parameters. In addition, for a fixed set of values of the passive elements involved in the circuit model, the choice of the threshold current I_{TH} within a feasible statistical range, does not appreciably weight upon the quenching time assessment.

On the other hand, since the diode current $i_{Rd}(t)$ linearly increases with V_{OV} through the term I_f, for a given I_{TH} level, the quenching time logarithmically depends on the overvoltage.

C. Recharging Operation

The third and last phase of the SiPM output response arises at the switch's closing point, after time $t = T$ from the detected event, and lingers on until the diode voltage $v_d(t)$ recovers to the external bias condition, and all circuit capacitances entirely recharge to their pre-existing quiescent values.

A correct assessment of the SiPM output current during the recovery transition, when no current flows through $R_{d,Nf}$, must properly take into account the voltage values collected across the circuit capacitors at time $t = T$, namely $V_{Ceq}(T)$, $V_{Cd}(T)$, and $V_{Cq}(T)$, since the sole contribution to the final transient of the output current through R_L is provided by the charge stored in the memory elements of the circuit at that instant. Fig. 18 depicts the linearized model describing the evolution of the output current throughout the recharging process, where the left branch including $R_{d,Nf}$ is opened and the initial conditions of capacitances $C_{d,Nf}$, $C_{q,Nf}$ and C_{eq} are modeled by series step-function voltage sources of amplitude equal to the voltages across them at the quenching time T, which are given by

$$V_{C_d}(T) = V_{OV} - R_d i_{R_d}(T) \tag{32}$$

$$V_{C_q}(T) = R_L i_{R_L,1}(T) + R_d i_{R_d}(T) - V_{OV} \tag{33}$$

$$V_{C_{eq}}(T) = R_L i_{R_L,1}(T) \tag{34}$$

while the related charges are respectively $Q_{Cd}(T) = C_{d,Nf}V_{Cd}(T)$, $Q_{Cq}(T) = C_{q,Nf}V_{Cq}(T)$, and $Q_{Ceq}(T) = C_{eq}V_{Ceq}(T)$.

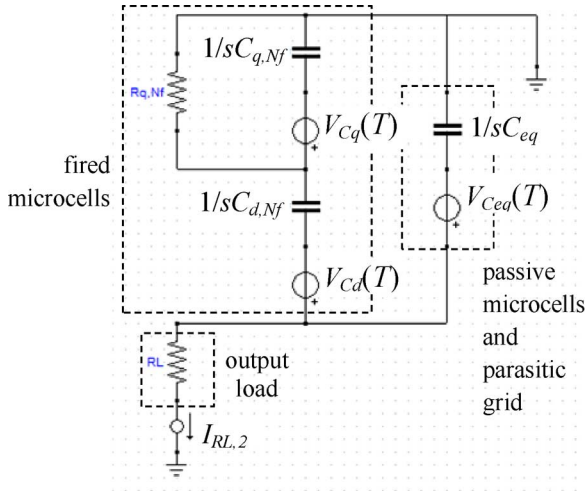

Fig. 18. Simplified small-signal Laplace-domain circuit used for evaluating the SiPM output current frequency response for the recharging operation.

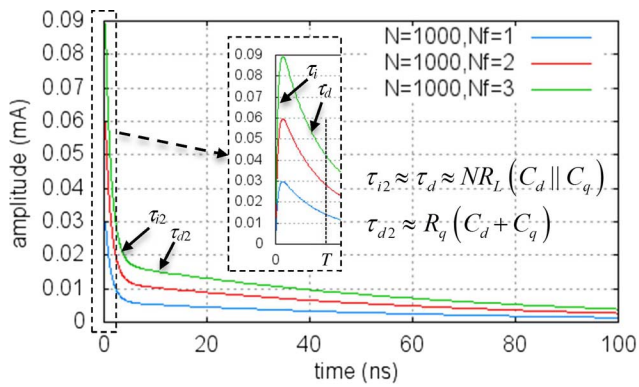

Fig. 19. Complete analytical SiPM output current waveforms upon a 50-Ω load resistor, for $V_{OV} = 2$ V, $I_{TH} = 100$ μA, $N = 1000$, and increasing values of N_f ($R_d = 300$ Ω, $R_q = 300$ kΩ, $C_d = 200$ fF, $C_q = 20$ fF, $C_m = 5$ fF).

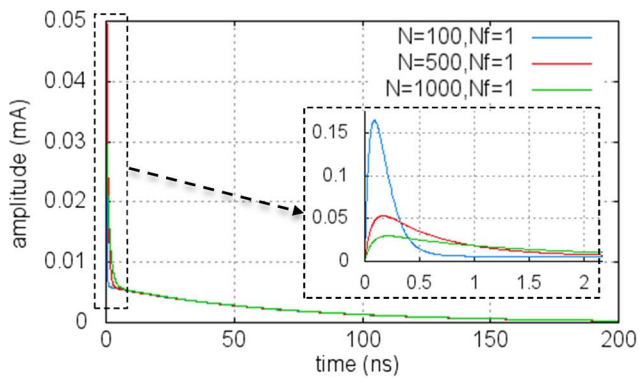

Fig. 20. Complete analytical SiPM output current waveforms upon a 50-Ω load resistance, for $V_{OV} = 2$ V, $I_{TH} = 100$ μA, $N_f = 1$, and different growing values of N ($R_d = 300$ Ω, $R_q = 300$ kΩ, $C_d = 200$ fF, $C_q = 20$ fF, $C_m = 5$ fF). It is found that the surface area beneath the curves is constant regardless of the total number of microcells.

Evaluating the small-signal transfer functions for every input source generator and applying the superimposition principle to the linear system in Fig. 18, yields the Laplace-domain expression

$$I_{R_L,2}(s) = H_{02}\frac{1 + s\tau_{q2}}{(1 + s\tau_{i2})(1 + s\tau_{d2})} \tag{35}$$

where $H_{02} = Q_{Ceq}(T) + Q_{Cd}(T)$, and

$$\tau_{q2} = \frac{\left[\tau_q Q_{C_d}(T) + \tau' Q_{C_q}(T) + \tau'' Q_{C_{eq}}(T)\right]}{H_{02}} \tag{36}$$

also being $\tau' = R_q C_d$ and $\tau'' = R_q(C_d + C_q)$.

Inverse Laplace transforming relationship (35) entails

$$i_{R_L,2}(t) = \frac{H_{02}}{\tau_{d2} - \tau_{i2}}\left(\frac{\tau_{q2} - \tau_{i2}}{\tau_{i2}} e^{-\frac{t-T}{\tau_{i2}}} - \frac{\tau_{q2} - \tau_{d2}}{\tau_{d2}} e^{-\frac{t-T}{\tau_{d2}}}\right) \tag{37}$$

representing the SiPM output response function for $t > T$.

Unlike the $i_{RL,1}(t)$ current in (10), $i_{RL,2}(t)$ is a monotonically decreasing curve starting from the initial value $i_{RL,2}(T)$, which equals $i_{RL,1}(T)$ for continuity, and exponentially declining with different time constants compared to those in the first part of the current response.

A first-order assessment of the recovery time constants can be performed with the same approach as in (12)–(17), giving

$$\tau_{i2} \approx \frac{a_2'}{a_1'} \approx \frac{NR_qR_LC_dC_d}{R_q(C_d + C_q) + NR_L(C_d \| C_q)} \tag{38}$$

$$\tau_{d2} \approx a_1' \approx R_q(C_d + C_q) + NR_L(C_d \| C_q) \tag{39}$$

As the term $R_q(C_d + C_q)$ is predominant in both above relationships, due to the typically high value of the quenching resistance, it turns out that τ_{i2} has a rather similar expression as the quenching time constant τ_d in (17), with a comparable behavior as in Fig. 10, while τ_{d2} is found to assume a considerably higher value, which is almost independent on N and N_f.

Combining relationships (10) and (37), the SiPM complete output current expression is obtained as a function of time

$$i_{R_L}(t) = \begin{cases} i_{R_L,1}(t), & 0 \le t \le T \\ i_{R_L,2}(t), & t \ge T \end{cases} \tag{40}$$

Fig. 19 depicts the related analytical current waveforms for $V_{OV} = 2$ V, $N = 1000$, and increasing values of N_f, illustrating the time constants characterizing the response transient evolution.

Time constant τ_{d2} is considered one of the most significant parameters of the SiPM response, since it defines the recovery time of the SPAD microcells. In fact, the photodiode voltage takes nearly $5\tau_{d2}$ to recover the correct bias conditions within 1% of the final value, and any incoming photon arriving prior to this time, which can even be ranged in the order of microseconds, has a lower avalanche triggering probability.

All current functions get almost linearly increased with N_f, thus confirming the direct proportionality of the SiPM output signals with the incident photon flux. Furthermore, the charge associated to the detected photons, for a fixed value of N_f, is independent of the overall number of cells N, as also shown in Fig. 20, where the complete SiPM current pulses are graphed for $V_{OV} = 2$ V, $I_{TH} = 100$ μA, $N_f = 1$, and growing values of N. The surface area underneath the curves is found to keep constant regardless of N. In addition, it is found that the recovery time constant linearly grows with N and does not depend on N_f.

The amount of charge Q_{TOT} released by an absorbed photon is represented by the surface area delimited by the diode current function i_{Rd} from the initial avalanche trigger instant until the

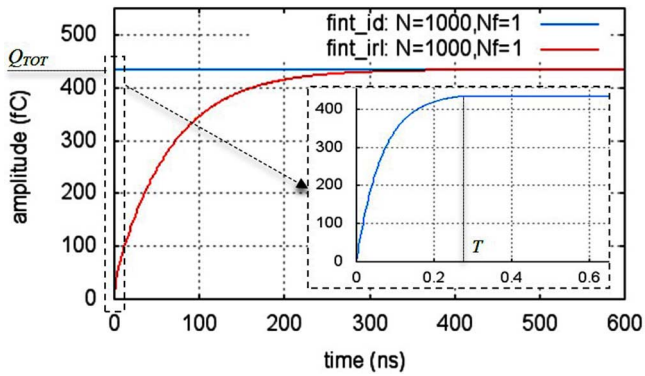

Fig. 21. Analytical waveforms of the instantaneous charges beneath the i_{Rd} and i_{RL} current pulse functions for $V_{OV} = 2$ V, $I_{TH} = 100$ μA, $N = 1000$, and $N_f = 1$ ($R_d = 300\ \Omega$, $R_q = 300$ kΩ, $C_d = 200$ fF, $C_q = 20$ fF, $C_m = 5$ fF). The total output pulse charge is essentially due to the SiPM recharge operation.

quenching time T, as clearly outlined in Fig. 3. The charge collected across the diode terminals is then provided as a current signal through the load resistor for the entire output pulse duration. As a consequence,

$$Q_{TOT} = \int_0^T i_{R_d}(t)dt = \int_0^{+\infty} i_{R_L}(t)dt \tag{41}$$

To further corroborate the developed analysis, the instantaneous charges contained within both $i_{Rd}(t)$ and $i_{RL}(t)$ analytical current pulses, that is $Q_{iRd}(t)$ and $Q_{iRL}(t)$, respectively, are here reported in Fig. 21 for $V_{OV} = 2$ V, $N = 1000$, and $N_f = 1$.

As expected, the integral function of i_{Rd} exponentially rises to the final value with the fastest time constant, τ_i, within the quenching time T. As soon as the total charge Q_{TOT} is reached, no current flows through the fired diode microcells and $Q_{iRd}(t)$ remains constant over the ensuing time.

Instead, the dynamic increase of the charge enclosed in the output current i_{RL} is predominantly determined by the slowest time constant of the circuit, τ_{d2}, so that $Q_{iRL}(t)$ approaches the total pulse charge Q_{TOT} within the SiPM recovery time.

As also detected by the charge plots in Fig. 21, the amount of Q_{TOT} developed upon R_L during the first part of the output response is negligible. In other terms,

$$\int_0^{+\infty} i_{R_L}(t)dt = \int_0^T i_{R_L,1}(t)dt + \int_T^{+\infty} i_{R_L,2}(t)dt \approx \int_T^{+\infty} i_{R_L,2}(t)dt \tag{42}$$

IV. Experimental Results

Analytical and measured output pulse waveforms are compared together for a 3×3 mm^2 Hamamatsu MPPC device with 50-μm pitch size. Measurements are performed at the Catania astrophysical Observatory Laboratory for Detectors (COLD).

A PDL 200B pulsed diode laser is used to produce the trigger avalanche into the MPPC microcells. The laser radiation intensity is controlled such that only a few cells get fired for each event. Pulse waveforms are acquired on a Lecroy digital oscilloscope with a 2.5-GHz bandwidth, a 20-GS/s sampling rate, and an intrinsic 1-mV baseline noise.

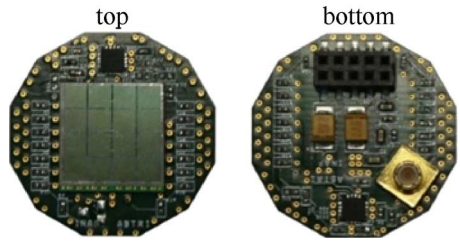

Fig. 22. Dedicated COLD test-board for the 3×3 mm^2 MPPC device.

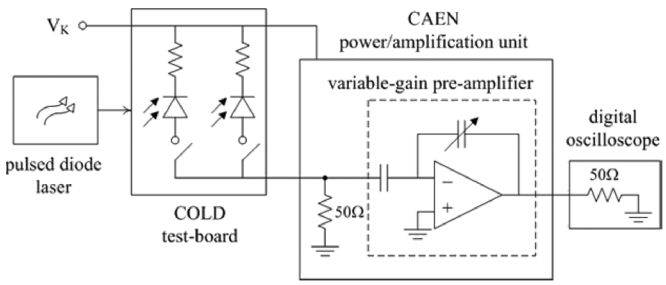

Fig. 23. Block diagram of the measurement set-up connections.

TABLE I
Extracted Model Parameter Values

	Hamamatsu MPPC (S11828-3344MX)					
	V_{BD} (V)	R_d (Ω)	R_q (Ω)	C_d (F)	C_q (F)	C_m (F)
Parameter values	70.5*	1k	290k	78f	8f	1f

*Evaluated at $T = 25.5$°C.

The laser pulses are set to be significantly shorter than the detector response time. Moreover, the frequency of the laser source flux is sufficiently small to allow a full recovery transition between two subsequent trigger events.

A dedicated test-board for the MPPC device is specifically developed to analyze the effects of increasing the total number of microcells on the shape of the obtained pulses. In fact, the board is equipped with a set of jumper pins providing the parallel anode connection of multiple 3×3 mm^2 macro-pixels. Fig. 22 shows the realized test-board. An appropriate mechanical interface is additionally implemented in order to allow the laser light to shine upon the detector surface.

The detector unit under test is connected to the input of an SP5600 CAEN power/amplification system with a 50-Ω input resistance and a tunable-gain pre-amplifier.

The measurement circuit connection diagram is reported in Fig. 23. All data are taken at room temperature.

Experimental measures are used to extract model parameter values as well as to validate the developed analytical analysis. Pulse shapes are compared through their peak amplitudes and overall charge collected.

For a fixed operating voltage, histograms of the maximum pulse amplitudes are digitally captured according to the number of cells firing for each event. Afterwards, events with the same number of fired cells are grouped together and averaged to form a single pulse waveform.

TABLE II
ANALYTICAL AND EXPERIMENTAL COMPARISON OF PULSE WAVEFORMS*

	Hamamatsu MPPC (S11828-3344MX)											
	1-pixel 3x3mm^2 (N=3600)						2-pixel 3x3mm^2 (N=7200)					
	N_f=1		N_f=2		N_f=3		N_f=1		N_f=2		N_f=3	
	Analyt.	*Meas.*	*Analyt.*	*Meas.*	*Analyt.*	*Meas.*	*Analyt.*	*Meas.*	*Analyt.*	*Meas.*	*Analyt.*	*Meas.*
Voltage peak amplitude (mV)	18.2	13.1	36.1	26.8	53.2	41.9	10.1	8.5	20.8	18.1	31.5	27.1
Current pulse charge (pC)	6.92	7.02	13.93	14.14	21.03	21.28	6.93	7.06	13.96	14.22	21.08	21.36

* Analytical and measured values refer to $R_L = 50\ \Omega$, and $V_{OV} = 1.3$ V.

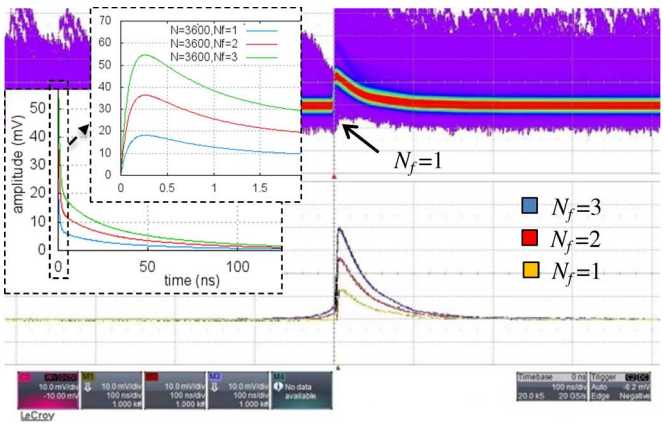

Fig. 24. Analytical and experimental pulse waveforms, for $N = 3600$ and increasing values of N_f.

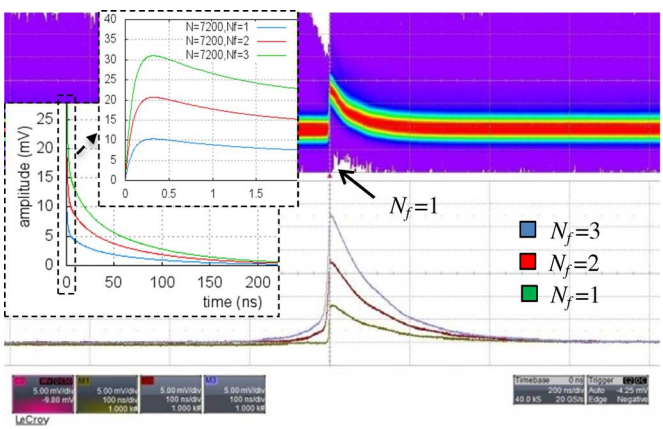

Fig. 25. Analytical and experimental pulse waveforms, for $N = 7200$ and increasing values of N_f.

Model parameters extraction is accomplished by means of an effective characterization procedure. In particular, the photodiode resistances are obtained from the slope of the forward I-V static characteristics; the charge delivered after a Geiger discharge is derived by applying a linear fit to the peak positions in a signal charge histogram; and the total microcell capacitance and breakdown voltage are respectively determined from the slope and x-axis intercept of the associated curve relating the measured charge to the external operating voltage. Table I summarizes the extracted values for the 3×3 mm^2 Hamamatsu macro-pixel device.

Based on the obtained V_{BD}, the external bias voltage V_K is regulated in order to achieve an overvoltage $V_{OV} = 1.3$ V, ensuring a Geiger-mode operation of the MPPC detector.

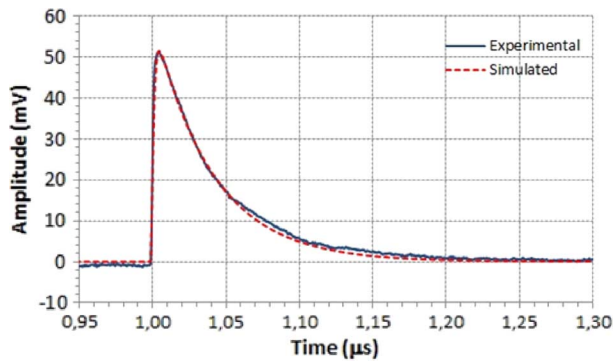

Fig. 26. Simulated and experimental output pulse waveform comparison, for $N = 3600$ and a single firing cell.

Analytical and experimental pulse waveforms are plotted in Fig. 24 and Fig. 25 for increasing values of the fired cells, respectively for $N = 3600$ and $N = 7200$.

The voltage peak amplitude and the current pulse charge of the obtained pulses are compared in Table II.

All analytical pulse functions are scaled by considering the current-to-voltage conversion operated by the load resistance and by also accounting for a 36-dB pre-amplifier gain factor.

The pre-amplifier somewhat shapes the original signal, due to its limited frequency bandwidth compared to the full spectral content of the MPPC pulses. As a result, the curve peaks are slightly reduced and their maximum amplitudes are consequently smoothed. However, the slowest part of the transient responses is not limited by the amplifier bandwidth, and the total current pulse charge, which is proved to be mainly released during the recharging operation, is in good accordance with the analytical results.

For each group of measures, a good linearity is obtained for increasing values of the firing cells.

In order to take into account the frequency shaping in the rising edge of the measured signals and achieve a more accurate comparison of the pulse waveforms, the electrical model of the SiPM detector is simulated and the SPICE model of the CAEN voltage pre-amplifier in Fig. 23 is additionally included in the simulation model cascaded to the output load. For a single firing cell, data outputs of the simulated and measured pulses are merged together into a single plot; Fig. 26 shows the resulting pulses, for $N = 3600$, and for a 1.3-V overvoltage and a 50-dB pre-amplifier gain. As inspected, both simulated and measured waveforms are well-overlapped even during the fast phase of their transient responses.

V. Conclusion

A systematic theoretical analysis of an accurate SiPM electrical model is carefully addressed to validate and predict the SiPM output response, with the aim of promoting additional understanding and encouraging improved development design of this class of solid-state detectors. The adopted model allows for an accurate analytical analysis of the device behavior. Analytical and experimental comparisons of the output pulse responses are performed to demonstrate the predictive capabilities of the adopted analysis. Measurements results of the SiPM output pulse waveforms as a function of time are in good agreement with expectations. By means of the proposed validated analysis, the main characteristics of the SiPM read-out signal can be profitably related to the front-end electronic detection system.

Acknowledgment

The authors are sincerely grateful to the referees of this paper for their valuable and helpful comments and suggestions.

References

[1] G. Condorelli, D. Sanfilippo, G. Valvo, M. Mazzillo, D. Bongiovanni, A. Piana, B. Carbone, and G. Fallica, "Extensive electrical model of large area silicon photomultipliers," *Nucl. Instrum. Meth. Phys. Res. A*, vol. 654, pp. 127–134, 2011.

[2] S. Cova, M. Ghioni, A. Lacaita, C. Samori, and F. Zappa, "Avalanche photodiodes and quenching circuits for single-photon detection," *Appl. Opt.*, vol. 35, no. 12, pp. 1959–1976, 1996.

[3] F. Corsi, A. Dragone, C. Marzocca, A. Del Guerra, P. Delizia, N. Dinu, C. Piemonte, M. Boscardin, and G. F. Dalla Betta, "Modelling a Silicon Photomultiplier (SiPM) as a signal source for optimum front-end design," *Nucl. Instrum. Meth. Phys. Res. A*, vol. 572, pp. 416–418, 2007.

[4] F. Corsi, C. Marzocca, A. Perrotta, A. Dragone, M. Foresta, A. Del Guerra, S. Marcatili, G. Llosa, G. Collazzuol, G. F. Dalla Betta, N. Dinu, C. Piemonte, G. U. Pignatel, and G. Levi, "Electrical characterization of silicon photomultiplier detectors for optimal front-end design," in *Proc. IEEE Nucl. Sci. Symp. Conf. Rec.*, 2006, pp. 1276–1280.

[5] N. Pavlov, G. Mæhlum, and D. Meier, "Gamma spectroscopy using a silicon photomultiplier and a scintillator," in *Proc. IEEE Nucl. Sci. Symp. Conf. Rec.*, 2005, pp. 173–180.

[6] S. Seifert, H. T. van Dam, J. Huizenga, R. Vinke, P. Dendooven, H. Löhner, and D. R. Schaart, "Simulation of silicon photomultiplier signals," *IEEE Trans. Nucl. Sci.*, vol. 56, no. 6, pp. 3726–3733, 2009.

[7] K. A. Wangerin, G.-C. Wang, C. Kim, and Y. Danon, "Passive electrical model of silicon photomultipliers," in *Proc. IEEE Nucl. Sci. Symp. Conf. Rec.*, 2008, pp. 1276–1280.

[8] A. G. Stewart, V. Saveliev, S. J. Bellis, D. J. Herbert, P. J. Hughes, and J. C. Jackson, "Performance of 1- mm^2 silicon photomultiplier," *IEEE J. Quantum Electron.*, vol. 44, no. 2, pp. 157–164, 2008.

[9] D. Marano, G. Bonanno, M. Belluso, S. Billotta, A. Grillo, S. Garozzo, G. Romeo, O. Catalano, G. La Rosa, G. Sottile, D. Impiombato, and S. Giarrusso, "Improved SPICE electrical model of silicon photomultipliers," *Nucl. Instrum. Meth. Phys. Res. A*, vol. 726, pp. 1–7, 2013.